Sensors & Actuators: B. Chemical 314 (2020) 128095

Contents lists available at ScienceDirect

Sensors and Actuators B: Chemical

journal homepage: www.elsevier.com/locate/snb

Liquid metal circuit based magnetoresistive strain sensor with discriminating magnetic and mechanical sensitivity

Tao Hu, Shouhu Xuan*, Li Ding, Xinglong Gong*

CAS Key Laboratory of Mechanical Behavior and Design of Materials, Department of Modern Mechanics, CAS Center for Excellence in Complex System Mechanics, University of Science and Technology of China, Hefei 230027, PR China

ARTICLE INFO

Keywords:
Liquid metal
Strain sensor
Mechanic-magnetic sensitive
Magnetorheological elastomer

ABSTRACT

This work reported a stretchable, magneto-sensitive and discriminative strain sensor consisting of liquid metal (LM) as the electronic circuit and carbonyl iron particles (CIPs)/polydimethylsiloxane (PDMS) composite as the packaging material (LME-MRE). Due to the good elasticity of PDMS matrix and unique magnetic interactions among CIPs, the LME-MRE sensor was both sensitive to the external mechanical and magnetic stimuli. Moreover, owing to the fluidic nature of liquid metal, LME-MRE sensor also exhibited good electrically healing capability. The relative resistance variation ($\Delta R/R_0$) of LME-MRE sensor reached as high as 1038 % under 40 % compressive strain. The electrical properties of LME-MRE sensor also remarkably changed under cyclic stretching and bending. Moreover, a 7.4 % decrement of resistance was achieved under applying a 300 mT magnetic field to LME-MRE sensor. Importantly, the magnetic and mechanical stimuli could be discriminated by LME-MRE sensor and a possible mechanism was proposed to describe the mechanic-electric-magnetic sensing characteristics. Finally, a LME-MRE sensor array is developed for the detection of both compressive force and magnetic field, demonstrating a broad promising in future intelligent devices, like artificial electronic skins and soft robotics.

1. Introduction

Due to the increasing requirements of flexible electronic devices, such as flexible sensors, artificial electronic skins, stretchable displays and wearable electronics, the flexible and stretchable electronics have attracted significant attention [1–11]. To replace the traditional rigid electrical conductors, various types of soft and conductive composites were fabricated and employed in practical applications thanks to their multidirectional deformability and controllable conductivity. During the fabrication process, there were two common methods to achieve the highly conductive, stretchable and flexible features. The first one was mixing conductive fillers such as carbon nanotubes [3,12,13], graphene [4,14–16] and metallic micro-particles or nanowires [17–19] into the elastomeric substrate. The second method was the formation of conductive laminated structures containing the conductive layer and stretchable substrate, for example, wavy metal lines or patterns on pre-strained substrate [20–22], conductive networks polymer film [23–28] and rigid electronic components integrated with soft substrate [29–31]. However, the rigid conductive layer would be damaged under large mechanical stimuli, which lead to the decrease of conductivity. The hybrid integration of rigid conductive layer and soft substrate would weaken the stretchability and flexibility of sensor, then further hinder its ultimate utility in practical application like wearable and flexible electronics.

Recently, the liquid phase conductive fillers such as ionic liquid and liquid metal initiated a new way to fabricate all-soft sensors with good shape reconfigurability, stable conductivity and healing capability. No rigid components were required so that the all-soft sensor could be easily compatible with the human body or other environments. Especially, the liquid metal has been in extremely interests thanks to the high electrical and thermal conductivity, negligible toxicity, low vapor pressure and controllable melting point [32–37]. As compared with other conductive liquid like ionic liquid, the oxide layer formed on the surface of liquid metal helped to maintain its shape, so that the devices could suffer less from the leakage if they were broken. Then the all-soft sensors with laminated structures and liquid metal patterns were developed [38–43]. Among the manufacturing processes, the polydimethylsiloxane (PDMS) based liquid metal sensors have been demonstrated to be good sensors due to their good mechanical strength and deformability, arbitrary molding capability and high light transmittance. Usually, liquid metal patterns were printed or encapsulated in PDMS substrate and then sealed with a PDMS cover. Such fabrication process produced ideal flexible and stretchable sensors because the sensors could respond to the external stimuli like stretching, pressing,

* Corresponding authors.
E-mail addresses: xuansh@ustc.edu.cn (S. Xuan), gongxl@ustc.edu.cn (X. Gong).

https://doi.org/10.1016/j.snb.2020.128095
Received 23 November 2019; Received in revised form 2 April 2020; Accepted 4 April 2020
Available online 10 April 2020
0925-4005/

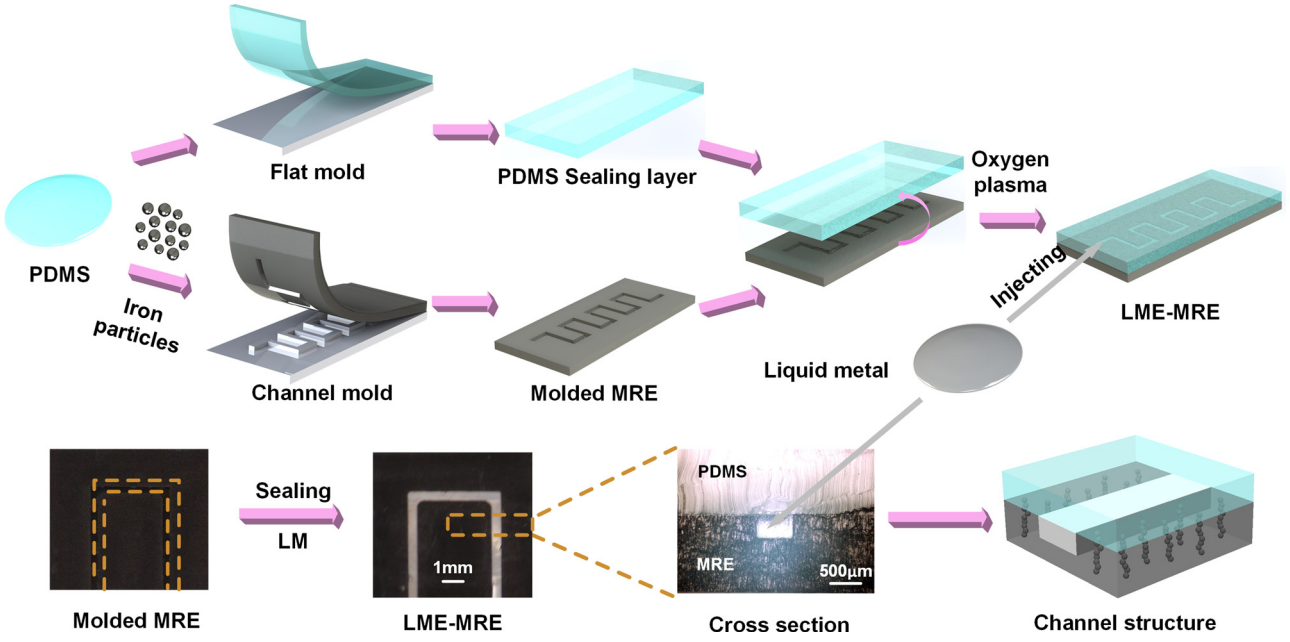

Fig. 1. The fabrication processes and digital images of LME-MRE.

bending and twisting. However, the complicated fabrication and single functionality confined the further development of these sensors. In order to further explore the liquid-solid coupling sensing behavior and practical application of these sensors, more facile and convenient approaches to develop high performance PDMS based liquid metal sensors were in pursuit.

Nowadays, sensors were often employed under complex environment, thus they needed the capability to tolerate and discriminate various stimuli. For example, the magnetic sensor would suffer from the high heat generation of the electromagnetic devices. For example, the pressure sensor should avoid the influence of triboelectric and tribothermal effect while it contacted with other objects. To this end, the sensors integrated with functional composites like magnetoelectric and thermoelectric material were developed. Among these materials, magnetorheological elastomers (MREs), consisting of magnetic particles and non-magnetic elastomeric matrix comprising silicone rubber, natural rubber and polyurethane, possessed typical mechanic-magnetic coupling properties [44–48]. The magnetic particles were concentrated to column-like structures and then fixed in the polymeric matrix. The mechanical properties of MREs were significantly influenced by magnetic interactions among the particle chains. Owing to the particular magnetic-induced properties, MREs could be employed as a magnetic sensor [47,48]. According to the soft nature and magneto-sensitivity of MREs, the integration between MREs and PDMS based liquid metal sensors would be beneficial for fabricating stretchable, flexible and magnetoresistive sensors with high sensing performance.

In this paper, liquid metal patterns were encapsulated in the channel structures of carbonyl iron particles (CIPs) doped PDMS matrix by a pure PDMS layer. The MRE with liquid metal (LME-MRE) possessed the advantages of simple fabrication, versatility, multidirectional deformability, good durability, electrically healing capability, strain and magnetic field dependent conductivity. Then the mechanic-electric-magnetic coupling properties of LME-MRE sensor were systematically investigated. The LME-MRE sensor could not only characterize the external strain and stress, but also detect the magnetic field. Surprisingly, it could further discriminate the applied mechanical and magnetic stimuli. Additionally, a possible mechanism was proposed to analyze the details of the mechanic-electric-magnetic coupling behavior. Finally, a smart writing board was constructed by the LME-MRE sensor arrays. The good sensing performance further demonstrated its feasibility toward the future sensing devices.

2. Experiment and characterization

2.1. Materials and preparation

Firstly, the carbonyl iron particles (CIPs, type CN, BASF) were fully mixed with the PDMS (Sylgard 184, Dow Corning GmbH) precursor and curing agent (weight ratio 20:1) for 10 min as magnetorheological (MR) precursor. The weight fraction of CIPs was set as 10 wt%, 30 wt% and 60 wt% to avoid the formation of cluster. Then the MR precursor was treated by ultrasonic cleaner and vacuum oven for 5 min to homogeneously separate CIPs and remove the bubbles. The MR precursor was cured in channel structured molds for 25 min under 80 ℃ with the dimension of 50 mm × 15 mm × 1 mm, to make MRE with channel structures inside. During the curing process, 1 T magnetic field was applied perpendicularly to the molds to form the CIP chains by a magnetic power system (IGLF-150, Beijing Saidi New Electromechanical Technology Co., China). Besides, the pure PDMS with weight ratio of 15:1 was cured for 20 min under 80 ℃ as the sealing layer (50 mm × 15 mm × 2 mm) and a hole puncher was used to produce through-vias in the sealing layer. Then the PDMS sealing layer was bonded with molded MRE substrate by oxygen-plasma treatment. Then GaInSn liquid metal (LM, melting point 16 ℃) was injected into channel structures (10 cm in length, 500 μm in width and 300 μm in thickness) by syringes and connected with copper wires through the vias on PDMS sealing layer. Finally, the vias were sealed by cured PDMS (Fig. 1).

2.2. Characterization

The morphology of LME-MRE was characterized by scanning electron microscope (SEM, Gemini 500, Carl Zeiss Jena Germany) and the digital images were taken by digital camera (D1700, Nikon) and digital microscope (KEYENCE VHX Digital Microscope, VH-Z100). Hysteresis Measurement of Soft and Hard Magnetic Materials (HyMDC Metis, Leuven, Belgium) and a rheometer (Physica MCR 301, Anton Paar Co., Austria) were employed to test the magnetic properties of MRE. A dynamic mechanical analyzer (DMA, ElectroForce 3200, TA instruments, Minnesota 55344 USA) was utilized to supply the tensile and

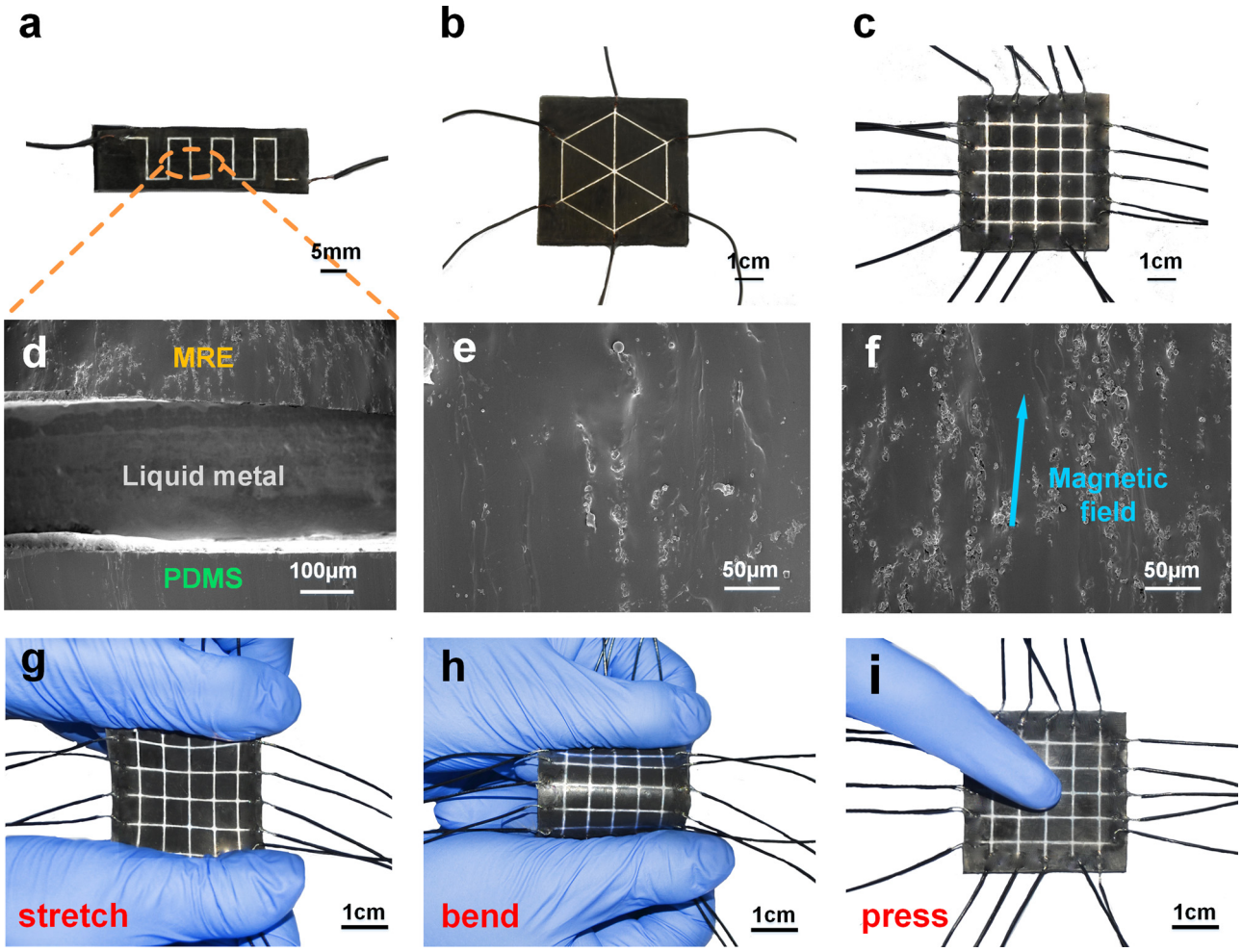

Fig. 2. Digital images of the liquid metal patterns inside MRE substrate: (a) strain sensor, (b) hexagon array and (c) 5 × 5 square array; SEM images of (d) channel structure, MRE substrate with CIP content of (e) 10 wt% and (f) 60 wt%; digital images of a LME-MRE array under various mechanical deformation: (g) stretching, (h) bending and (i) pressing.

compressive force to the LME-MRE sensor. The sensor was connected with the Modulab® material test system (Solartron analytical, AMETEK advanced measurement technology, Inc., United Kingdom) to evaluate the electrical performance. In addition, a DC power supply (ITECH IT6724), commercial electromagnet and permanent NdFeB magnet were employed to generate magnetic field, and the magnetic flux density was measured by a Tesla meter (HT20, Shanghai Hengtong magnetic technology Co. Ltd, China).

3. Results and discussion

3.1. Design of LME-MRE

To validate the capability of the LME-MRE, the design of LME-MRE with complex liquid metal patterns was demonstrated (Fig. 2a–c). In these patterns, the channel structures were fully filled with liquid metal that no obvious defect was observed in straight channels and sharp corners, which showed the reliability of LME-MRE.

In Figs. 1 and 2d, the clear interface between PDMS sealing layer and MRE substrate indicated that the channel structures were successfully formed. The smooth light area inside the channel clarified that liquid metal was totally encapsulated without leakage. Moreover, the CIP chains were embedded in the PDMS matrix and aligned along the applied magnetic field (Fig. 2e,f). Undoubtedly, by increasing the CIP content, the chain-like structures in the matrix obviously increased. Under the magnetic field, the magnetic induced properties of LME-MRE were enhanced by stronger particle interactions. So the mechanic-electric-magnetic coupling properties of LME-MRE sensors were depended on the CIP content. The LME-MRE sensor arrays possessed good flexibility under various mechanical stimuli, such as stretching, bending and pressing (Fig. 2g–i). So the highly flexible LME-MRE sensors with complex liquid metal patterns were fabricated, which was a new approach of all-soft and magneto-sensitive sensor.

Interestingly, the iron particles and liquid metal endowed LME-MRE sensor with unique magnetic properties and electrically healing capability. Here, the MRE substrate with different CIP content were tested by HyMDC to evaluate the magnetic properties. The saturation magnetization was 20.3 emu/g, 55.9 emu/g and 110.5 emu/g for MRE with CIP content of 10 wt%, 30 wt% and 60 wt%, respectively (Fig. 3a). The variation tendency of saturation magnetization was coincident with CIP content of MRE, which reflected the stable magnetization performance of CIPs inside the MRE substrate. Under the shear frequency of 5 Hz and strain amplitude of 0.1 %, the shear storage modulus G of MRE evidently increased with the magnetic field, which showed typical magnetorheological effect of MRE (Fig. 3b). By increasing the CIP content from 10 wt% to 30 wt% and 60 wt%, the initial modulus G_0 and magnetic induced modulus $G_m = G - G_0$ significantly increased, which proved the enhancement of magnetic induced properties. Afterwards, a light emitting diode (LED), Arduino breadboard and power module were employed to establish a constant voltage circuit to show the healing capability of stretchable liquid metal circuit. The LME-MRE sensor was severed with scissors and healed electrically for several

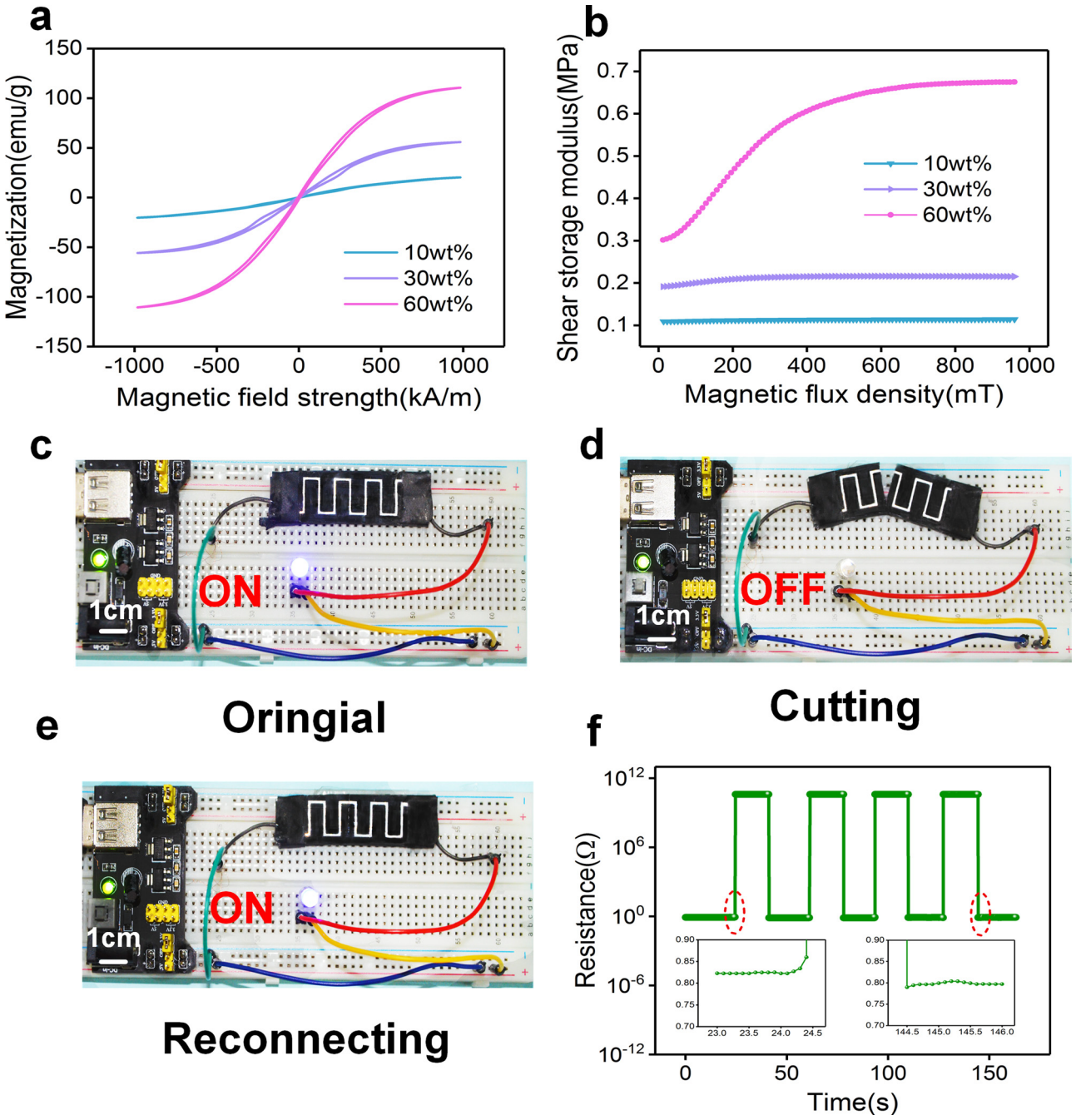

Fig. 3. (a,b) Magnetization curves and storage modulus of MRE substrate with CIP content of 10 wt%, 30 wt% and 60 wt%; (c–e) digital images of LME-MRE sensor integrated with breadboard and LED: cut and reconnection, scale bar: 1 cm; (f) the corresponding resistance variation of LME-MRE sensor.

times under ambient conditions (Fig. 3c–e). The brightness of LED could be remained after the reconnection. Because the initial resistance of LME-MRE sensor was 0.82 Ω, and after reconnection it was 0.79 Ω (Fig. 3f).

3.2. Mechanic-electric coupling properties of LME-MRE sensor

One of the main requirements for flexible sensors was to maintain their electrical functionality during the deformation. In order to systematically evaluate the mechanic-electric coupling properties, the sensing performance of LME-MRE sensor with 60 wt% CIP content MRE substrate was tested by applying cyclic compressive and tensile force. To investigate the compressive behavior, a 3D-printed plastic bar (bottom area: 4 mm × 4 mm, Flashforge, ltd, China) was prepared to compress the surface of LME-MRE perpendicularly, for the simulation of a finger (Fig. 4a). Then the compressive test system, consisting of the DMA, the 3D-printed bar and an electromagnet was established. Two signal lines were employed to deliver the electrical signals from sensor to Modulab system.

Here, the compressive strain with cyclic sine waveform was applied to the LME-MRE sensor and no current was applied to the electromagnet to keep the same test environment with magnetic-compressive coupling test. The resistance variation was defined as $\Delta R = R - R_0$, R_0 was the initial resistance. Keeping the compressive frequency at 0.5 Hz, the R quickly increased from 0.81 Ω to 9.21 Ω under 40 % compressive strain, for which $\Delta R/R_0$ reached 1038 %. Due to the Mullis effect, the MRE substrate was strain softened, which resulted in the initial peak value of resistance. So the $\Delta R/R_0$ and compressive force of later stable

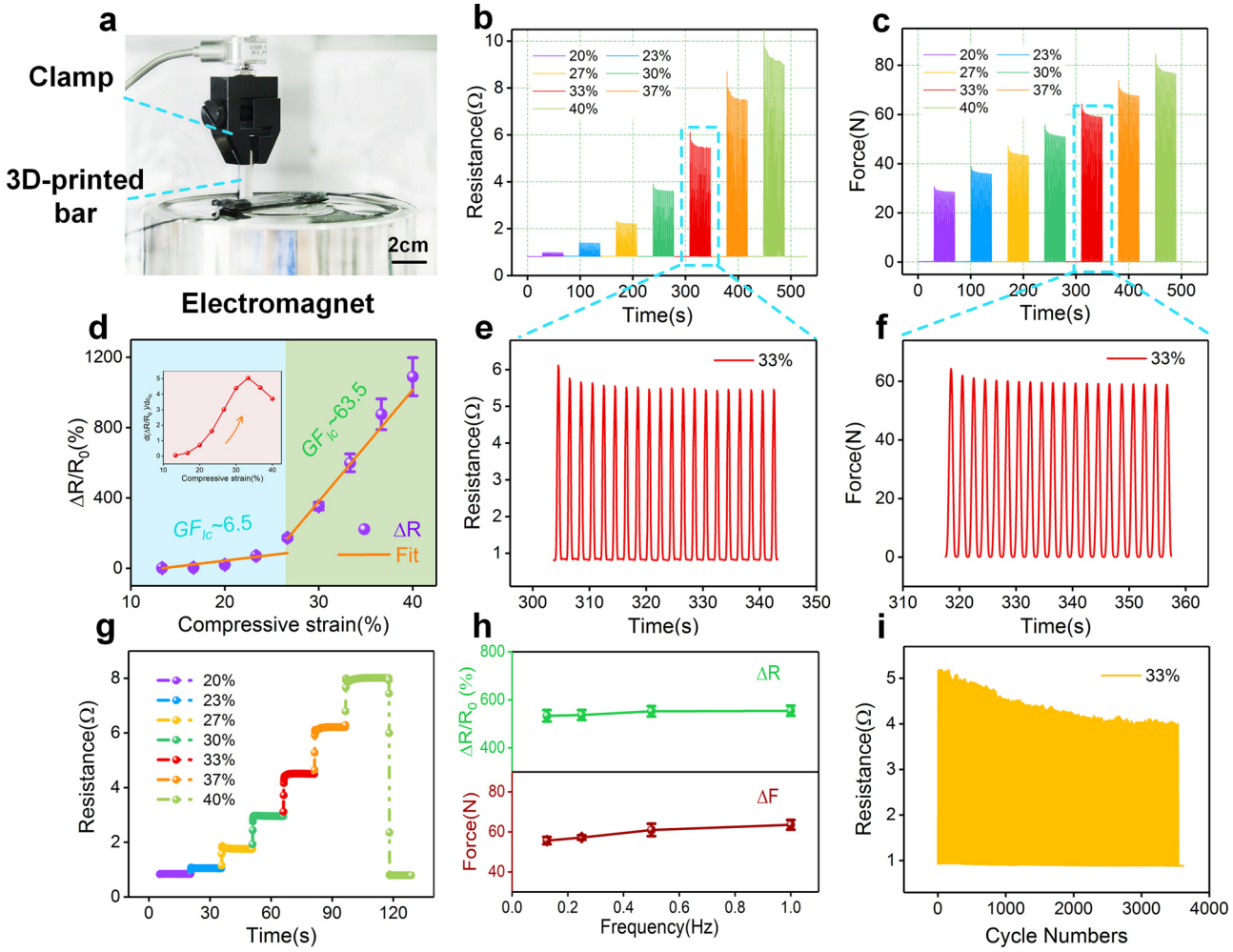

Fig. 4. (a) Digital images of the cyclic compressive test system: clamp of DMA, 3D-printed bar, electromagnet, scale bar: 2 cm; (b,c) the compressive strain dependent resistance and force of LME-MRE sensor at the compressive frequency of 0.5 Hz; (d) initial value and first derivative of $\Delta R/R_0$ versus compressive strain; (e,f) typical resistance and force under the compressive strain amplitude of 33 %; (g) the ΔR under step by step loading with increasing compressive strain; (h) the resistance and force versus compressive frequency under the compressive strain amplitude of 33 %; (i) the stability under cyclic compressive loading.

cycles were collected here. They could accurately return to the original state after each 20 compress-release cycles, demonstrating the good repeatability. When the compressive strain amplitude varied from 20 % to 40 % with the increment of 3.33 %, the ΔR gradually enhanced (Fig. 4b). The $\Delta R/R_0$ versus compressive strain for the loading and unloading phases with the amplitude of 33 % have shown the low hysteresis of LME-MRE sensor (Fig. S2a). The electrical properties of LME-MRE mainly relied on the dimension of the liquid metal circuit inside. $R = \rho l/s$, ρ was the resistivity of liquid metal, l was the length and s was the cross-sectional area. The higher the compressive displacement, the tighter the LME-MRE was compressed, the smaller the channels. Thanks to the liquidity of GaInSn, it would easily deform within compressed channels. Then the s decreased, which led to the increase of R. During the unloading phase, the bar was removed, hence the deformation of channels recovered and the resistance decreased.

Meanwhile, it was also observed that the compressive force presented the same variation tendency with compressive strain. Under various compressive strain amplitude, the maximum compressive force enhanced from 28.5 N to 76.7 N (Fig. 4c). Especially, both the electrical and mechanical signals under the compressive strain amplitude of 33 % exhibited good stability (Fig. 4e.f). Here, the initial thickness of sensor D_0 was 3.0 mm and the compressive displacement varied from 0.4 mm to 1.2 mm with increment of 0.1 mm. The local compressive strain ε_{lc} was defined as $\Delta D/D_0$, the direction was along the thickness in which ΔD was the variation of thickness. In order to further evaluate the sensing performance of LME-MRE sensor, the gauge factor (GF_{lc}) was calculated by $\frac{\Delta R/R_0}{\varepsilon_{lc}}$. Clearly, GF_{lc} could be divided into two parts (blue and green region) with different variation tendency and the corresponding compressive strain was 13%–25% and 25%–40%. After being fitted, the GF_{lc} reached as high as 6.5 ± 1.1 and 63.5 ± 4.1 in blue and green region, respectively. The increasing $\frac{d(\Delta R/R_0)}{d\varepsilon_{lc}}$ further indicated the enhancement of sensitivity (Fig. 4d). In the low compressive strain region (blue region), the 3D-printed bar slightly compressed with the surface of PDMS sealing layer and the deformation of the sealing layer was small, so the dimension of channels under the sealing layer also changed a little, thus the resistance of LME-MRE increased slowly. Then in the green region, this area of LME-MRE sensor was squeezed so hard by the plastic bar, hence the channels had a large deformation and the resistance significantly increased. In the stress-strain curve, the hysteresis loop showed the typical viscoelasticity of LME-MRE. And the variation tendency of compressive stress was consistent in each cycle, which represented the good repeatability (Fig. S3). Under step loading, the compressive displacement changed from 0.6 mm to 1.2 mm with the increment of 0.1 mm, and the dwell time was 15 s (Fig. 4g). The resistance of LME-MRE sensor was stable under each compressive strain, so the noise in the sensor response showed few influence on the sensing performance.

Moreover, the compressive frequency also hardly affected the electrical properties of LME-MRE sensor. After the compressive strain

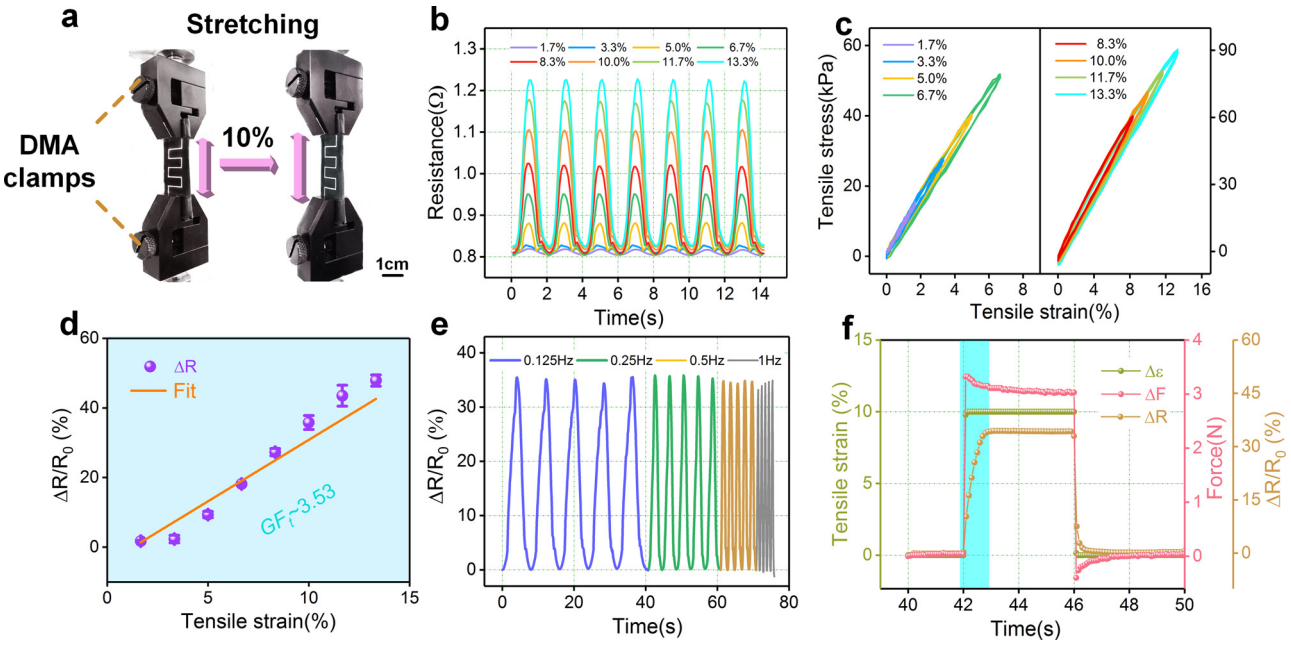

Fig. 5. (a) Digital images of the cyclic tensile test system, scale bar: 1 cm; (b,c) the tensile strain dependent resistance and force of LME-MRE sensor at the tensile frequency of 0.5 Hz; (d) $\Delta R/R_0$ versus tensile strain; (e) $\Delta R/R_0$ at various tensile frequency under the tensile strain amplitude of 10 %; (f) the electrical and mechanical response of LME-MRE sensor under tensile strain with square waveform.

amplitude was set at 33 %, R could be kept stable during the loading-unloading phases under different compressive frequency (0.125 Hz, 0.25 Hz, 0.5 Hz and 1 Hz). The compressive force was recorded synchronously which possessed similar variation tendency with R (Fig. 4h). As the stability of sensing devices was essential in practical application, a continuous cyclic test was conducted by compressing the LME-MRE sensor under 0.5 Hz and 1 mm for 3500 cycles (Fig. 4i). Although the reduction of electrical response in 3500 cycles was about 21.9 %, the conductivity change was only 5.3 %, which was relatively small. The results of cyclic compressive tests demonstrated that LME-MRE could be employed in sensing devices due to good sensitivity.

To further explore the potential of LME-MRE in sensing devices, the tensile strain sensing performance was tested. During the test, the LME-MRE sensor was fixed with the clamps of DMA (stretch area: 30 mm × 15 mm), and tested under tensile strain with cyclic sine waveform (Fig. 5a). The R increased by 33.7 % with the sensor was stretched by 10 %. And the corresponding tensile stress reached 71 ± 0.5 kPa with little hysteresis (Fig. 5b,c). Both the mechanical and electrical performance of LME-MRE sensor recovered in each stretch-release cycle. The $\Delta R/R_0$ versus tensile strain for the loading and unloading phases with the amplitude of 10 % further showed the little hysteresis of LME-MRE sensor (Fig. S2b). Here, the gauge factor GF_t was calculated by $\frac{\Delta R/R_0}{\varepsilon_t}$, $\varepsilon_t = \Delta l/l_0$, ε_t was the tensile strain along the length of sensor, Δl and l_0 was the variation and initial value of length.. The sensitivity of LME-MRE sensor under cyclical tensile strain was 3.53 ± 0.2 with the fit coefficient of 0.972 by fitting (Fig. 5d). The $\Delta R/R_0$ gradually increased with the elongation of sensor, demonstrated its feasibility in tensile sensing.

Afterwards, the electrical responses of LME-MRE sensor at various tensile frequency were investigated (Fig. 5e). The $\Delta R/R_0$ was stable at 0.125 Hz, 0.25 Hz, 0.5 Hz and 1 Hz under tensile strain amplitude of 10 %, respectively. The results indicated the performance of LME-MRE sensor was hardly affected by the tensile frequency, which was similar to cyclic compressive test. Furthermore, the tensile strain with square waveform was employed to evaluate the responsive behavior of LME-MRE sensor (Fig. 5f). When the DMA clamp suddenly moved up for 3 mm, the instantaneous tensile force reached 3.32 N. However, the liquid metal circuit slowly deformed inside the stretched channels, so R also gradually raised (the blue region). Then the clamp dwelled, the tensile force and $\Delta R/R_0$ kept at a balanced value (3.1 N and 34 %). During the unloading phase, a similar and symmetrical variation could be found on the mechanical and electrical response of LME-MRE sensor. The stable tensile sensing performance made LME-MRE an ideal candidate for sensing devices.

The high flexibility of MRE substrate and soft nature of liquid metal endowed LME-MRE sensor with good bending properties. For cyclic bending test, compressive strain with cyclic sine waveform was applied to compress the end of sensor, which made the LME-MRE bent. Here, the bending angle θ at the middle was defined as the difference between the inclination of LME-MRE upper and lower part, and the bending angle α at the two sides was defined as the rotation of upper and lower part from the central axis (Fig. 6a). The larger the compressive displacement, the greater the θ and α. The ΔR of LME-MRE sensor was indeed due to the bending at the middle and two sides of sensor. However, the upper and lower part was short and almost flat, so $\approx 2\alpha$, and the θ could be used to represent the global bending of LME-MRE sensor. After keeping the test frequency at 0.5 Hz, the R increased by 20 % with θ from 0 to 70 °, for which the variation tendency was similar to cyclic compressive and tensile tests (Fig. 6b). As θ increased, the deformation of both the channel structures and liquid metal was larger, which led to larger variation of electrical properties. The $\Delta R/R_0$ reached 1.1 %, 5.4 %, 10.0 % and 20.7 % while the θ kept at 10 °, 30 °, 50 ° and 70 °. The $\Delta R/R_0$ versus θ for the loading and unloading phases with the amplitude of 60 ° exhibited the little hysteresis of LME-MRE sensor in cyclic bending (Fig. S2c). At the same time, the GF_f ($\frac{\Delta R/R_0}{\Delta\theta}$, $\Delta\theta$ was the variation of bending angle) gradually increased and the fitted results exhibited that the sensitivity was enhanced from blue to green region (Fig. 6c).

The electrical performance of LME-MRE sensor was barely impacted by the bending frequency. Kept the bending frequency at 0.125 Hz, 0.25 Hz, 0.5 Hz and 1 Hz, the $\Delta R/R_0$ slightly varied as 14.4 %, 14.0 %, 13.6 % and 13.5 % under 60°, which still conformed with the conclusion in cyclic compressive and tensile tests (Fig. 6d). The variation of bending force was also synchronously recorded to evaluate the mechanical performance of LME-MRE sensor. Furthermore, after bending for 3000 cycles under 60 ° and 0.5 Hz, the R virtually recovered in each

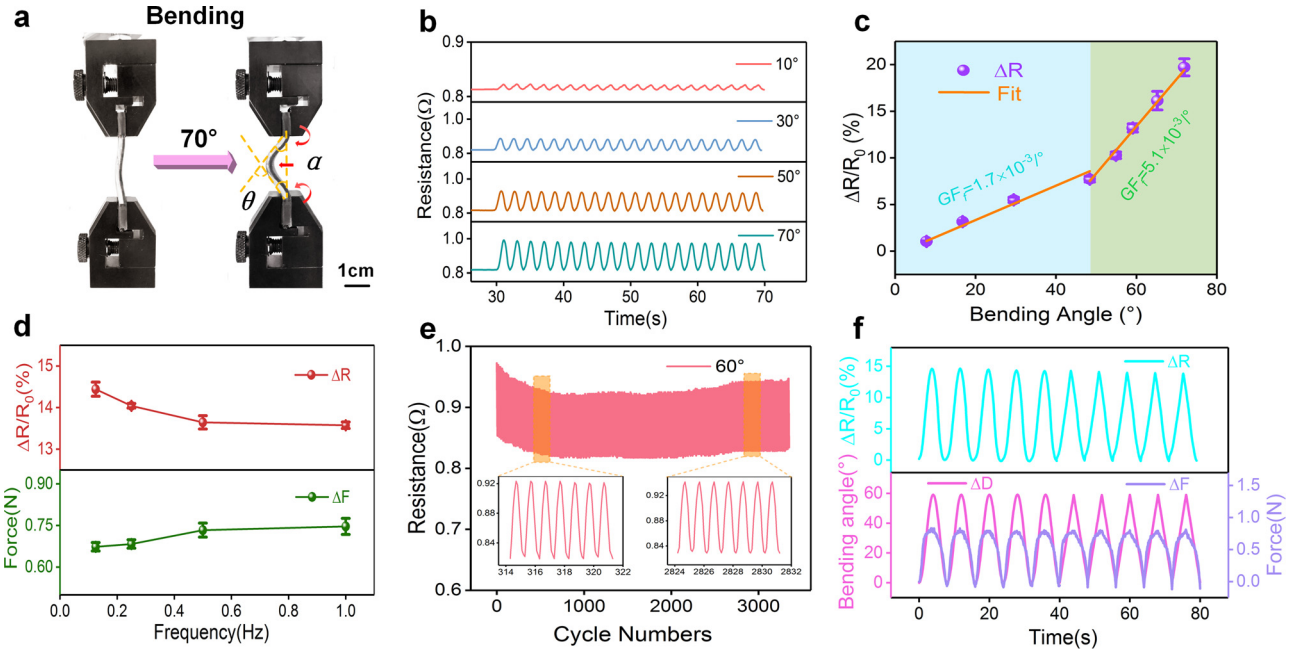

Fig. 6. (a) Digital images of the cyclic bending test system, scale bar: 1 cm; (b) the bending angle dependent resistance of LME-MRE sensor at bending frequency of 0.5 Hz; (c) $\Delta R/R_0$ versus bending angle; (d) the resistance and force at various bending frequency under the bending angle of 60°; (e) the stability under cyclic bending; (f) the electrical and mechanical response of LME-MRE sensor under bending with cyclic sine and triangle waveform.

bend-release cycle, which proved the good stability of LME-MRE sensor (Fig. 6e). Moreover, the kind of loading waveform could be discriminated by the LME-MRE sensor. When cyclic sine or triangle waveform was applied, the R_0 and ΔR kept consistent in each cycle, showing same variation tendency with the loading, which further demonstrated the feasibility of LME-MRE sensor (Fig. 6f).

3.3. Magnetic-electric coupling properties of LME-MRE sensor

Because of the particle interactions among numerous CIP chains embedded in PDMS matrix (Fig. 2d–f), LME-MRE possessed unique magnetic-induced capabilities. It could synchronously deform and recover as the magnetic field is applied and removed. Here, the LME-MRE sensors containing MRE substrate with CIP content of 10 wt%, 30 wt% and 60 wt% were tested, marked as X wt% LME-MRE sensor. During the test, the current with cyclic sine or square waveform was applied to electromagnet and LME-MRE sensor was placed on the center of electromagnet (Fig. 7a). By varying the current amplitude from 1 to 2, 3, 4 and 5 A, the maximum magnetic flux density generated by the electromagnet increased from 100 mT to 200 mT, 300 mT, 350 mT and 400 mT.

By applying cyclic magnetic field with the amplitude of 300 mT and period of 6 s, the R of 60 wt% LME-MRE sensor ranged from 0.81 Ω to 0.75 Ω, for which the variation tendency was interestingly contrary to the results under cyclic mechanical stimuli (Fig. 7b). Clearly, the absolute value of ΔR gradually increased with magnetic flux density. The $\Delta R/R_0$ versus magnetic flux density for the loading and unloading phases with the amplitude of 350 mT also showed the little hysteresis of LME-MRE sensor (Fig. S2d). By increasing the CIP content from 10 wt% to 30 wt% and 60 wt%, the absolute value of GF_m ($\frac{\Delta R/R_0}{\Delta B}$, ΔB was the variation of magnetic flux density) dramatically increased, and the corresponding magnetic sensitivity enhanced from 0.05 to 0.08 and $0.19 \pm 0.01\ \mathrm{mT}^{-1}$ (Fig. 7c). A mechanism was proposed to describe the magnetic-electric coupling sensing performance of LME-MRE sensor (Fig. 7g). Under the external magnetic field, the channel structures inside MRE substrate deformed into concave shape due to the magnetostriction of MRE substrate, hence the bottom of liquid metal became convex, both the width d and length l of liquid metal patterns decreased. The resistance of liquid metal $R = \rho l/s$ and the volume of liquid metal $V = l \times s$, so $R = \rho l/s = \rho l^2/V$. During the test, the resistivity ρ and volume V was unchanged, so the decrease of l resulted in the decrease of R. The higher the CIP content, the more the CIPs chains were formed (Fig. 2e–f). Thus the particle interactions were also augmented, which led to the larger magnetic-induced deformation of LME-MRE and higher magnetic sensitivity.

Moreover, the cyclic magnetic-compressive coupling test was conducted to validate the ability of LME-MRE sensor to discriminate magnetic and mechanical stimuli. The test environment of cyclic magnetic-compressive coupling test was the same as cyclic compressive test. At first, the sensor was compressed by the 3D-printed bar with no current was applied to electromagnet. After one compressive cycle, the bar was dwelled and the current with sine waveform was applied to electromagnet for one cycle, then the process was repeated. The $\Delta R/R_0$ under compressive displacement of 0.4 mm and magnetic field of 100 mT was 3% and −3% (Fig. 7d). The electrical response of LME-MRE sensor to compressive force and magnetic field was contrary, so the kind of stimuli could be easily discriminated. By increasing of compressive strain or magnetic flux density, the absolute value of ΔR both increased, which was consistent with the results in cyclic compressive and magnetic field tests. After applying magnetic field with cyclic square waveform for 400 cycles, the electrical properties of LME-MRE sensor were still stable in each on-off cycle, which further proved the good stability (Fig. 7e). Finally, magnetic field with cyclic sine and square waveform could be discriminated by the LME-MRE sensor. The good responsive performance further demonstrated its potential in sensing components (Fig. 7f).

3.4. Application of LME-MRE sensor

The experiments showed that the LME-MRE sensor possessed both good mechanical and magnetic sensing performance, which made it an ideal candidate for flexible sensors. In order to further illustrate the applicability of LME-MRE, the LME-MRE sensor was integrated on gloves to detect the finger motion, and LME-MRE sensor arrays were developed for the detection of compression and external magnetic field. The MRE with the CIP content of 60 wt% and the dimension of

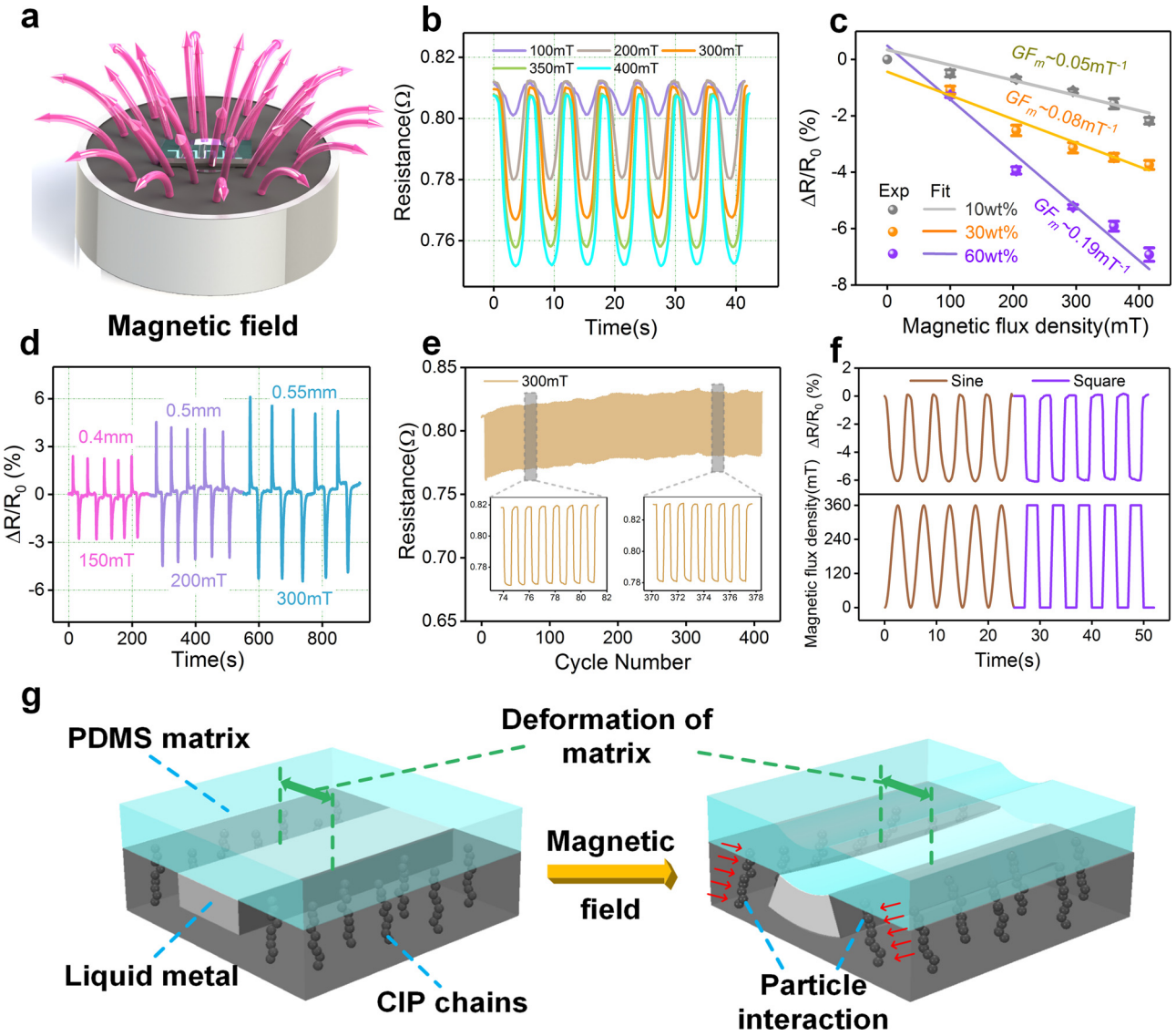

Fig. 7. (a) Schematic illustration of the electromagnet and LME-MRE sensor; (b) the magnetic field dependent resistance of LME-MRE sensor with the period of 6 s; (c) $\Delta R/R_0$ versus magnetic flux density; (d) $\Delta R/R_0$ under cyclic magnetic-compressive coupling loading; (e) the stability under cyclic magnetic field; (f) the response of LME-MRE sensor under magnetic field with sine and square waveform; (g) schematic illustration of the magnetic-electric coupling sensing mechanism.

50 mm × 50 mm × 1 mm was selected as the substrate for sensor arrays. The channel structures inside the MRE substrate was 500 μm in width and 300 μm in thickness.

By integrating the LME-MRE sensor on the gloves, the motion of finger could be recorded (Fig. 8a,b). When bending the finger, the LME-MRE sensor was also synchronously stretched. With the increase of bending angle θ, the $\Delta R/R_0$ gradually enhanced, then $\Delta R/R_0$ recovered after the finger was outspread. By moving a permanent NdFeB magnet to the center of 3 × 3 LME-MRE sensor array, the corresponding 2D intensity profile of $\Delta R/R_0$ showed the distribution of applied magnetic field (Fig. 8c,d). During the process, the bottom of channel structure kept at a convex shape by the attracting of permanent magnet. Then length l of liquid metal patterns increased, which caused the increase of R. This electrical response was contrary to the cyclic magnetic field test because the electromagnet generated an opposite magnetic attractive force under the LME-MRE sensor. What's more, the LME-MRE sensor could be used as a smart writing board (Fig. 8e). When writing on the 5 × 5 LME-MRE sensor array, the liquid metal circuit under the stylus pen significantly deformed, which led to the increase of R. And the R of other areas remained constant. Fig. 8f presented the handwritten word of "L" in light and dark green. The larger the compressive force, the greater the ΔR, showing the darker color than other areas. Thanks to the mechanic-magnetic detection ability, the LME-MRE was proved for the feasibility in future electronic devices.

4. Conclusion

In summary, the LME-MRE sensor consisting of channel structured PDMS/CIPs composite and liquid metal circuit was developed. The CIPs formed chain-like structures parallel to magnetic field in the MRE substrate. During the loading and unloading phases, the liquid metal deformed with the channel structures inside MRE substrate. The strain sensor based on LME-MRE was proved to have good sensing performance under mechanical stimuli like pressing, stretching and bending. Moreover, the responsive performance of LME-MRE sensor was synchronously influenced by the external magnetic field, which indicated that it was able to be used as magneto-resistive sensor. Especially, the magnetic and mechanical stimuli could be discriminated by the different responses of LME-MRE sensor. Finally, the LME-MRE was developed to smart sensor arrays for mechanic-magnetic detection. Hence, the good mechanical properties and unique sensing performance of LME-MRE guaranteed that it could be widely used in future

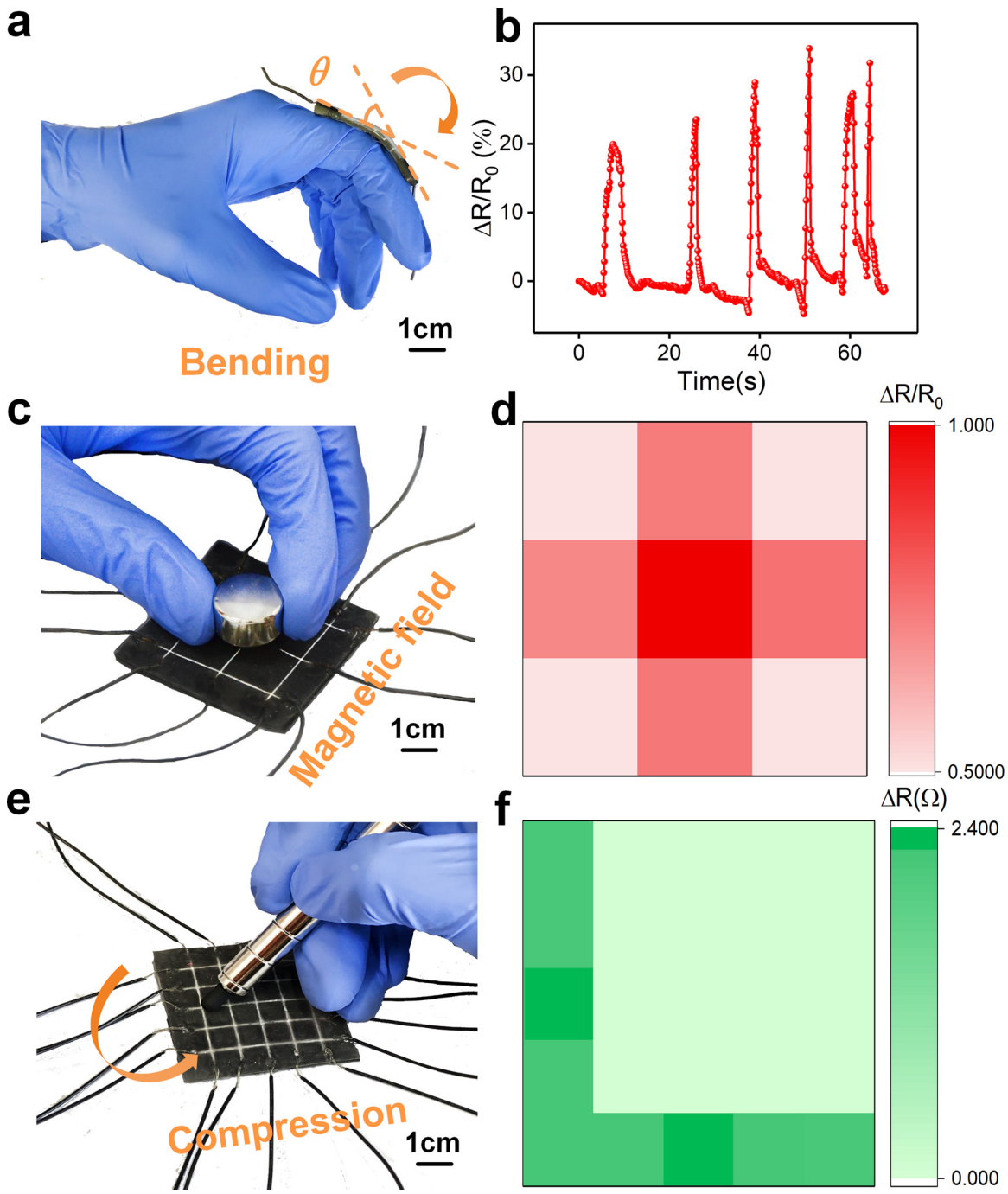

Fig. 8. (a,b) Digital images of LME-MRE sensor integrated on gloves and corresponding $\Delta R/R_0$ when bending the finger; digital images of LME-MRE sensor array and corresponding 2D intensity profile of $\Delta R/R_0$: (c,d) moving a permanent NdFeB magnet to the middle of sensor array; (e-f) writing an "L" on the sensor array by stylus pen, scale bar:1 cm.

intelligent sensing devices.

Declaration of interests

The authors declare that they have no known competing financial interests or personal relationships that could have appeared to influence the work reported in this paper.

CRediT authorship contribution statement

Tao Hu: Investigation, Formal analysis, Validation, Writing - original draft, Writing - review & editing. **Shouhu Xuan:** Conceptualization, Writing - review & editing. **Li Ding:** Writing - review & editing. **Xinglong Gong:** Supervision.

Acknowledgement

Financial supports from the National Natural Science Foundation of China (Grant Nos. 11822209) and Strategic Priority Research Program of the Chinese Academy of Sciences (Grant No. XDB22040502) are gratefully acknowledged. This work is also supported by the Collaborative Innovation Center of Suzhou Nano Science and Technology.

Appendix A. Supplementary data

Supplementary material related to this article can be found, in the online version, at doi:https://doi.org/10.1016/j.snb.2020.128095.

References

[1] B.W. An, S. Heo, S. Ji, F. Bien, J.U. Park, Transparent and flexible fingerprint sensor array with multiplexed detection of tactile pressure and skin temperature, Nat. Commun. 9 (2018) 2458.
[2] A.P. Tjahyono, K.C. Aw, J. Travas-Sejdic, A novel polypyrrole and natural rubber based flexible large strain sensor, Sens. Actuators B Chem. 166 (2012) 426–437.
[3] K.H. Kim, S.K. Hong, N.S. Jang, S.H. Ha, H.W. Lee, J.M. Kim, Wearable resistive pressure sensor based on highly flexible carbon composite conductors with irregular surface morphology, ACS Appl. Mat. Inter. 9 (2017) 17500–17508.
[4] Y. Pang, H. Tian, L.Q. Tao, Y.X. Li, X.F. Wang, N.Q. Deng, et al., Flexible, highly sensitive, and wearable pressure and strain sensors with graphene porous network structure, ACS Appl. Mat. Inter. 8 (2016) 26458–26462.
[5] H.R. Lim, H.S. Kim, R. Qazi, Y.T. Kwon, J.W. Jeong, W.H. Yeo, Advanced soft materials, sensor integrations, and applications of wearable flexible hybrid electronics in healthcare, energy, and environment, Adv. Mater. (2019) 1901924.
[6] S.H. Wu, P.H. Liu, Y. Zhang, H.N. Zhang, X.H. Qin, Flexible and conductive nanofiber-structured single yarn sensor for smart wearable devices, Sens. Actuators B Chem. 252 (2017) 697–705.
[7] T. Sekitani, H. Nakajima, H. Maeda, T. Fukushima, T. Aida, K. Hata, et al., Stretchable active-matrix organic light-emitting diode display using printable elastic conductors, Nat. Mater. 8 (2009) 494–499.
[8] L. Donaldson, Stretchable and foldable electronic displays, Mater. Today 16 (2013) 416-.
[9] Y.N. Ma, N.S. Liu, L.Y. Li, X.K. Hu, Z.G. Zou, J.B. Wang, et al., A highly flexible and sensitive piezoresistive sensor based on MXene with greatly changed interlayer distances, Nat. Commun. 8 (2017) 1207.
[10] K. Takei, T. Takahashi, J.C. Ho, H. Ko, A.G. Gillies, P.W. Leu, et al., Nanowire active-matrix circuitry for low-voltage macroscale artificial skin, Nat. Mater. 9 (2010) 821–826.
[11] B. Peele, S. Li, C. Larson, J. Cortell, E. Habtour, R. Shepherd, Untethered stretchable displays for tactile interaction, Soft Robot. 6 (2019) 142–149.
[12] L.H. Wang, L.H. Cheng, Piezoresistive effect of a carbon nanotube silicone-matrix composite, Carbon 71 (2014) 319–331.
[13] M. Amjadi, Y.J. Yoon, I. Park, Ultra-stretchable and skin-mountable strain sensors using carbon nanotubes-Ecoflex nanocomposites, Nanotechnology 26 (2015) 375501.
[14] C.S. Boland, U. Khan, G. Ryan, S. Barwich, R. Charifou, A. Harvey, et al., Sensitive electromechanical sensors using viscoelastic graphene-polymer nanocomposites, Science 354 (2016) 1257–1260.
[15] R. Moriche, M. Sanchez, A. Jimenez-Suarez, S.G. Prolongo, A. Urena, Strain monitoring mechanisms of sensors based on the addition of graphene nanoplatelets into an epoxy matrix, Compos. Sci. Technol. 123 (2016) 65–70.
[16] Y. Lin, S.Q. Liu, S. Chen, Y. Wei, X.C. Dong, L. Liu, A highly stretchable and sensitive strain sensor based on graphene-elastomer composites with a novel double-interconnected network, J. Mater. Chem. C Mater. Opt. Electron. Devices 4 (2016) 6345–6352.
[17] S. Aziz, K.C. Jung, S.H. Chang, Stretchable strain sensor based on a nanocomposite of zinc stannate nanocubes and silver nanowires, Compos. Struct. 224 (2019) 111005.
[18] S. Chen, Y. Wei, X. Yuan, Y. Lin, L. Liu, A highly stretchable strain sensor based on a graphene/silver nanoparticle synergic conductive network and a sandwich structure, J. Mater. Chem. C Mater. Opt. Electron. Devices 4 (2016) 4304–4311.
[19] S.H. Park, J. Park, H.N. Park, H.M. Park, J.Y. Song, Flexible galvanic skin response sensor based on vertically aligned silver nanowires, Sens. Actuators B Chem. 273 (2018) 804–808.
[20] S. Xu, Z. Yan, K.I. Jang, W. Huang, H.R. Fu, J. Kim, et al., Assembly of micro/nanomaterials into complex, three-dimensional architectures by compressive buckling, Science 347 (2015) 154–159.
[21] D.H. Kim, J.A. Rogers, Stretchable electronics: materials strategies and devices, Adv. Mater. 20 (2008) 4887–4892.
[22] M. Amjadi, A. Pichitpajongkit, S. Lee, S. Ryu, I. Park, Highly stretchable and sensitive strain sensor based on silver nanowire-elastomer nanocomposite, ACS Nano 8 (2014) 5154–5163.
[23] M. Tavakoli, M.H. Malakooti, H. Paisana, Y. Ohm, D.G. Marques, P.A. Lopes, et al., EGaIn-assisted room-temperature sintering of silver nanoparticles for stretchable, inkjet-printed, thin-film electronics, Adv. Mater. 30 (2018) 1801852.
[24] Z.Y. Liu, D.P. Qi, P.Z. Guo, Y. Liu, B.W. Zhu, H. Yang, et al., Thickness-gradient films for high gauge factor stretchable strain sensors, Adv. Mater. 27 (2015) 6230–6237.
[25] M.D. Ho, Y. Ling, L.W. Yap, Y. Wang, D. Dong, Y. Zhao, et al., Percolating network of ultrathin gold nanowires and silver nanowires toward "Invisible" wearable sensors for detecting emotional expression and apexcardiogram, Adv. Funct. Mater. 27 (2017) 1700845.
[26] Z. Chen, T. Ming, M.M. Goulamaly, H.M. Yao, D. Nezich, M. Hempel, et al., Enhancing the sensitivity of percolative graphene films for flexible and transparent pressure sensor arrays, Adv. Funct. Mater. 26 (2016) 5061–5067.
[27] X.Q. Liao, Z. Zhang, Q.J. Liang, Q.L. Liao, Y. Zheng, Flexible, cuttable, and self-waterproof bending strain sensors using microcracked gold nanofilms@paper substrate, ACS Appl. Mat. Inter. 9 (2017) 4151–4158.
[28] Y.X. Song, W.M. Xu, M.Z. Rong, M.Q. Zhang, A sunlight self-healable transparent strain sensor with high sensitivity and durability based on a silver nanowire/polyurethane composite film, J. Mater. Chem. A Mater. Energy Sustain. 7 (2019) 2315–2325.
[29] J. Yun, C. Song, H. Lee, H. Park, Y.R. Jeong, J.W. Kim, et al., Stretchable array of high-performance micro-supercapacitors charged with solar cells for wireless powering of an integrated strain sensor, Nano Energy 49 (2018) 644–654.
[30] G. Buettel, J. Joppich, U. Hartmann, Micromachined silicon cantilevers with integrated high-frequency magnetoimpedance sensors for simultaneous strain and magnetic field detection, Appl. Phys. Lett. 111 (2017) 232401.
[31] J. Yoon, S.Y. Hong, Y. Lim, S.J. Lee, G. Zi, J.S. Ha, Design and fabrication of novel stretchable device arrays on a deformable polymer substrate with embedded liquid-metal interconnections, Adv. Mater. 26 (2014) 6580–6586.
[32] M.D. Dickey, Stretchable and soft electronics using liquid metals, Adv. Mater. 29 (2017) 1606425.
[33] N. Kazem, T. Hellebrekers, C. Majidi, Soft multifunctional composites and emulsions with liquid metals, Adv. Mater. 29 (2017) 1605985.
[34] M.D. Bartlett, N. Kazem, M.J. Powell-Palm, X.N. Huang, W.H. Sun, J.A. Malen, et al., High thermal conductivity in soft elastomers with elongated liquid metal inclusions, Proc. Natl. Acad. Sci. U.S.A. 114 (2017) 2143–2148.
[35] A. Fassler, C. Majidi, Liquid-phase metal inclusions for a conductive polymer composite, Adv. Mater. 27 (2015) 1928–1932.
[36] D. Kim, Y. Lee, D.W. Lee, W. Choi, K. Yoo, J.B. Lee, Hydrochloric acid-impregnated paper for gallium-based liquid metal microfluidics, Sens. Actuators B Chem. 207 (2015) 199–205.
[37] P.M. Adhi, M. Kondo, M. Takahashi, Performance of solid electrolyte oxygen sensor with solid and liquid reference electrode for liquid metal, Sens. Actuators B Chem. 241 (2017) 1261–1269.
[38] J.B. Andrews, K. Mondal, T.V. Neumann, J.A. Cardenas, J. Wang, D.P. Parekh, et al., Patterned liquid metal contacts for printed carbon nanotube transistors, ACS Nano 12 (2018) 5482–5488.
[39] M.G. Kim, H. Alrowais, S. Pavlidis, O. Brand, Size-scalable and high-density liquid-metal-based soft electronic passive components and circuits using soft lithography, Adv. Funct. Mater. 27 (2017) 1604466.
[40] G.Y. Li, X. Wu, D.W. Lee, A galinstan-based inkjet printing system for highly stretchable electronics with self-healing capability, Lab Chip 16 (2016) 1366–1373.
[41] Y.L. Chen, Y. Nguyen, S.E. Wu, Y.C. Chun, C.S. Chuang, Y.P. Hsieh, et al., Patterned liquid metal contacts for high density, stick-and-peel 2D material device arrays, Nanoscale 10 (2018) 14510–14515.
[42] C.W. Park, Y.G. Moon, H. Seong, S.W. Jung, J.Y. Oh, B.S. Na, et al., Photolithography-based patterning of liquid metal interconnects for monolithically integrated stretchable circuits, ACS Appl. Mat. Inter. 8 (2016) 15459–15465.
[43] G.Y. Li, X. Wu, D.W. Lee, Selectively plated stretchable liquid metal wires for transparent electronics, Sens. Actuators B Chem. 221 (2015) 1114–1119.
[44] M. Asun Cantera, M. Behrooz, R.F. Gibson, F. Gordaninejad, Modeling of magneto-mechanical response of magnetorheological elastomers (MRE) and MRE-based systems: a review, Smart Mater. Struct. 26 (2017) 023001.
[45] S.B. Choi, W.H. Li, M. Yu, H.P. Du, J. Fu, P.X. Do, State of the art of control schemes for smart systems featuring magneto-rheological materials, Smart Mater, Struct. 25 (2016) 043001.
[46] S.S. Sun, D.H. Ning, J. Yang, H. Du, S.W. Zhang, W.H. Li, A seat suspension with a rotary magnetorheological damper for heavy duty vehicles, Smart Mater. Struct. 25 (2016) 105032.
[47] T. Hu, S.H. Xuan, L. Ding, X.L. Gong, Stretchable and magneto-sensitive strain sensor based on silver nanowire-polyurethane sponge enhanced magnetorheological elastomer, Mater. Des. 156 (2018) 528–537.
[48] L. Ding, S.H. Xuan, L. Pei, S. Wang, T. Hu, S.S. Zhang, et al., Stress and magnetic field bimode detection sensors based on flexible Cl/CNTs-PDMS sponges, ACS Appl. Mat. Inter. 10 (2018) 30774–30784.

Tao Hu received his B.S. degree in the Department of Modern Mechanics, University of Science and Technology of China (USTC) in 2016 and continued his research under the direction of Prof. Xinglong Gong in the Intelligent Materials and Vibration Control Laboratory. His research interests are focused on smart sensing materials and magnetically controllable devices.

Dr. Shouhu Xuan is a Professor of Engineering Science at the University of Science and Technology of China (USTC), Hefei, Anhui, P.R. China. He got the B.S. degree from Anhui Normal University (China) in 2003 and received the Ph.D. degree in Chemistry from USTC in 2008. After working as a Post-doc for 2 years at the Chinese University of Hong Kong, Hong Kong, he joined the Department of Modern Mechanics, USTC, in 2010. His research interests cover the smart materials and multifunctional nanoparticles. In smart materials, he focuses on the development of high performance magnetorheological (MR) materials such as MR fluids, MR elastomers, MR gels and investigation of their fundamental mechanisms. For multifunctional nanoparticles, he is interested in the design, characterization and application of magnetic nanocomposites, and magnetic nanostructures in nanocatalysis and nanomedicine.

Li Ding is currently a Ph.D. candidate in Department of Modern Mechanics at University of Science and Technology of China, Hefei, Anhui, P.R. China. She received her B.S. degree in Astronautic Engineering and Mechanics from Harbin Institute of Technology, Harbin, Heilongjiang, P.R. China in 2015.

Dr. Xinglong Gong is a Professor of Engineering Science at the University of Science and

Technology of China (USTC), Hefei, Anhui, P.R. China. He got his B.S. and Master degree in solid mechanics from USTC in 1988 & 1991, respectively. He received his Ph.D. degree in Mechanics from both the USTC and Saitama University (Japan), in 1996. Then, he worked at the Nihon Dempa Kogyo Co., Ltd., Japan, for 7 years, and was promoted from Engineer to Chief Engineer of HIC Design. In 2003, he joined the Department of Modern Mechanics, USTC, as a Full Professor. His research interests cover the soft matter materials including magnetorheoloical fluid, electrorheological fluid, magnetorheological elastomer, shear thicking materials, polymer nanocomposites, as well as their application in the vibration isolator, vibration absorber, anti-shock equipment, and body armor.